On the extension of k−ω−SST corrections to predict flow separation on thick airfoils with leading-edge roughness

Gutierrez, Ruben; Zamponi, Riccardo; Ragni, Daniele; Llorente, Elena; Aranguren, Patricia

DOI
10.1002/we.2822

Publication date
2023

Document Version
Final published version

Published in
Wind Energy

Citation (APA)
Gutierrez, R., Zamponi, R., Ragni, D., Llorente, E., & Aranguren, P. (2023). On the extension of k−ω−SST corrections to predict flow separation on thick airfoils with leading-edge roughness. *Wind Energy*, *26*(7), 650-667. https://doi.org/10.1002/we.2822

Received: 7 November 2022 | Revised: 6 March 2023 | Accepted: 6 April 2023
DOI: 10.1002/we.2822

RESEARCH ARTICLE

WILEY

On the extension of $k-\omega-SST$ corrections to predict flow separation on thick airfoils with leading-edge roughness

Ruben Gutierrez[1] | Riccardo Zamponi[2,3] | Daniele Ragni[2] | Elena Llorente[1] | Patricia Aranguren[4]

[1]Aerodynamics Blade Engineering Department in Nordex SE, Sarriguren, Spain
[2]Department of Flow Physics and Technology, Faculty of Aerospace Engineering, Delft University of Technology, Delft, The Netherlands
[3]Department of Environmental and Applied Fluid Dynamics, von Karman Institute for Fluid Dynamics, Sint-Genesius-Rode, Belgium
[4]Engineering Department, Public University of Navarre, Pamplona, Spain

Correspondence
Rubén Gutierrez, Aerodynamics Blade Engineering Department in Nordex SE, Avenida Ciudad de la Innovación 3, 31621, Sarriguren, Spain.
Email: RGutierrez@nordex-online.com

Abstract

Modern wind turbines employ thick airfoils in the outer region of the blade with strong adverse pressure gradients and high sensitivity to flow separation, which can be anticipated by leading-edge roughness. However, Reynolds average Navier-Stokes simulations currently overpredict the Reynolds shear stresses near the surface, and the flow separation is not correctly predicted. Hence, these methods are not representative enough to optimize the blade design to avoid flow separation, which becomes relevant for rough blades. While several eddy-viscosity corrections in the $k-\omega-SST$ turbulence model have been previously studied to predict flow separation over smooth airfoils, the present study aims to extend their applicability to airfoils with leading-edge roughness. Two corrections, whose effect on flow physics has not been empirically quantified, are addressed. Particle image velocimetry measurements have been performed on a 30% thick airfoil to quantify the impact of these corrections. The reduction of the eddy viscosity introduced by the corrections leads to a shift of the peak location of the Reynolds shear stresses away from the surface, which, in turn, promotes flow separation and improves the prediction of the mean velocity and the pressure-coefficient distribution. Besides, the ratio between the main turbulent shear stress and turbulent kinetic energy is demonstrated to be lower than the standard value used in the $k-\omega-SST$ turbulence model at the boundary-layer outer edge. Adjusting this ratio for an angle of attack of 0° decreases the error on the predicted lift and drag coefficients from 75% to 3% and from 58% to 39%, respectively.

KEYWORDS
aerodynamics, distributed roughness, flow separation, PIV, thick airfoils

1 | INTRODUCTION

In the range of megawatt wind turbines, the length of the blades has been increased from 22.8 m (Smith–Putnam wind turbine) to 108 m (Haliade-X wind turbine) in the last 80 years. This tendency has allowed the cost of energy (COE) to be lowered per wind turbine and the wind turbine to be adapted to multiple types of site conditions. However, long blades deflect relatively more from the rotor plane during operation, and

---

additional stiffness is thus required to avoid the collision of the blade tip with the tower. This stiffness could be reached with the addition of more composite layers, except that the blade mass would excessively increase with a dependency on the cube of the blade length. To reduce the weight of the blade while keeping the same stiffness, either high-modulus materials can be used, or the thickness of the outboard region of the blade can be increased.

Thick airfoils are known to be more sensitive to leading-edge (LE) roughness than thin ones.[1] The use of these airfoils at the outboard region of the blade would increase the sensitivity of the blades to roughness. As a result, the power production of wind turbines would decrease and, in turn, the annual energy production (AEP). Corten et al[2] justified AEP losses of up to 25% caused by insect contamination on a stall-regulated wind turbine. This loss of AEP has been reduced in modern wind turbines through pitch regulation or even special control schemes.[3]

Moreover, the shape of these thick airfoils implies an adverse pressure gradient (APG) higher than that for thin airfoils, which, in combination with the loss of momentum caused by LE-roughness within the BL, separates the flow for a wider range of angles of attack (AoAs). Timmer et al[4] observed that the lower surface of thick airfoils is even more sensitive to flow separation at negative AoAs than the upper surface at positive incidences. Gutierrez et al[5] demonstrated that LE roughness could induce flow separation on the pressure side (PS) of a 30% thick airfoil for low positive AoAs (AoA $\leq 5^\circ$). Additionally, Gutierrez et al[6] showed that this flow separation varies the lift and drag more substantially than for 25% and 18% thick airfoils. Hence, the blade conditions for which the flow separates must be suitably defined to avoid blade-loading problems and abrupt power losses.

Among the numerical techniques used to compute the aerodynamic coefficients of an airfoil, panel methods and Reynolds average Navier-Stokes (RANS) simulations are the most feasible ones for the industry. Nevertheless, these approaches are not able to predict flow separation at high APGs like those produced by thick airfoils, resulting in the wrong estimation of lift and drag forces. This has been widely demonstrated for airfoils with negligible flow effects due to roughness, often referred to as smooth airfoils. However, there has been no attempt in the literature to improve this limitation along with the modeling of LE roughness.

In particular, panel methods are known to be less computationally expensive than other numerical methods. Still, they overpredict the lift-to-drag ratio L/D for thick airfoils with an error of around $5\text{–}10\,\%$,[7] even for smooth-surface assumptions. Additionally, the drag error was shown to differ by about 20% between thick and thin airfoils.[8] Recently, Olsen et al[9] attempted to include the effects of LE roughness in a panel method, which was, however, only validated for the LE-roughness conditions of a 18% thick airfoil. Although several RANS studies focused on predicting LE-roughness effects for thin airfoils, [10,11] also the numerical prediction of flow separation on thick airfoils remains inaccurate, even for smooth surfaces. Sezer-Uzol et al[12] extensively reviewed CFD studies from 2001 to 2020 for wind-turbine airfoils at a Reynolds number of $Re > 10^6$. Most of these studies were performed under a steady 2D-RANS approach, obtaining a suitable prediction of force coefficients when the flow was attached but also an underprediction of the flow separation beyond the maximum lift. Sorensen et al[13] performed detached Eddy simulations (DES) of the 3D-replica of a wind-tunnel section equipped with a 18% thick airfoil and a similar underprediction of flow separation occurred. Thus, corrections for RANS approaches are still of interest for capturing flow separation. The RANS approach was indeed originally intended to model turbulent problems with small regions of flow separation and a limited range of turbulent length scales acting within them. In contrast, the relatively stronger APG associated with the shape of thick airfoils causes a separated-shear layer in the order of magnitude of the airfoil thickness.

The Reynolds shear stresses in RANS simulations are usually modeled through the Boussinesq assumption. Nevertheless, this method fails for flows with sudden changes in mean strain rate, three-dimensionality, and development over curved surfaces,[14] such as those developed on thick airfoils. As a result, the eddy viscosity (μ_t) and, in turn, the turbulent shear stresses are overestimated near the airfoil. Some efforts to correct this overestimation of shear stress in RANS turbulence models are the studies of Bangga et al.,[15] Matyushenko et al,[16] and Zhong et al.[17] These corrections aim to decrease μ_t near the airfoil and reduce the amplitude of the shear stresses. The methods of Matyushenko et al[16] and Zhong et al[17] tune a calibration coefficient of the $k-\omega-SST$ turbulence model to lower μ_t, while the technique of Bangga et al[15] multiplies μ_t by a constant factor in specific regions of interest. In their analysis, Matyushenko et al[16] used four airfoils with thicknesses ranging from 15% to 21%. The a_1 coefficient was varied to match the measured pressure-coefficient distribution C_p of an S809 airfoil at an AoA of 10°, a_1 being the ratio between the main turbulent shear stress and the turbulent kinetic energy. The default value of this coefficient in the $k-\omega-SST$ turbulence model is based on the observations of Bradshaw[18] and Townsend, [19] who demonstrated a_1 to be a constant value of 0.31 at the outer edge of a boundary layer under conditions of zero pressure gradient. However, Matyushenko et al[16] concluded that a value of a_1 equal to 0.28 provided the best agreement in the prediction of aerodynamic coefficients and was applied to the rest of the airfoils showing improvements at different Re. Their conclusion agrees with some studies mainly based on flat plate flows,[20–22] whose experimental analysis reported a drop in a_1 below 0.31 under APG conditions. Nevertheless, there is no empirical validation of this value on an airfoil that could justify the conclusions of Matyushenko et al,[16] and there is no knowledge about how this drop in a_1 differs from the APGs given by the thick airfoil of this study. On the other hand, the modification of a_1 will act within the entire fluid domain and may change the modeling of roughness provided by the boundary conditions, which is not studied by the literature.

The main drawback of the correction of a_1 is that the prediction of the skin-friction coefficient worsens in regions of flow attachment after its application.[16] This was even demonstrated to occur for flat-plate flows.[15] The above-mentioned correction of Bangga et al[15] avoids this interference with the prediction of the skin friction since their damping factor acts only on μ_t in the flow separation regions. The activation of this damping factor depends on a threshold linked to the inverse of a turbulent length scale. The values of this factor and length scale were selected to match the skin-friction measurements on a flat plate. Afterward, the method was applied to DU airfoils with thicknesses ranging from 25% to 40%. As a result, the error in lift and drag prediction was reduced, but the stall angle was still overestimated. In summary, both correction methods described above are based on certain APGs and were based on fully turbulent simulations without leading-edge roughness modeling. Hence, the reason for this failure still needs to be understood so that the corrections can be extended to predict other kinds of flow separations, such as that caused by the APG of thick airfoils downstream of the LE roughness.

As emphasized by Wu et al.,[23] LE roughness induces the flow transition at low *Re*, delaying separation. On the contrary, the rough elements trip the BL to a turbulent state at high *Re* and affect the near-wall velocity causing a momentum deficit, which produces the opposite effect. Some studies[24–26] aimed to explain how the flow separates over rough flat surfaces under APG flat-plate flows. They observed that the turbulent mixing, particularly the Reynolds shear stress $\overline{u'v'}$, is reduced near the separation point. As a result, the separation point is shifted upstream, and the shear layer is thicker than that on a smooth surface. Recently, the study of Beresh et al[27] showed that particle-image-velocimetry (PIV) data could be used to infer μ_t and, in turn, understand the prediction of the RANS equations. Zhang et al[28] performed PIV measurements on an airfoil with LE roughness and concluded that the turbulent kinetic energy is increased in the outer flow. Although the study of Zhang et al[28] also analyzed Reynolds shear stresses, no relation with RANS modeling was given.

The present study aims to quantify the failure of steady 2D-RANS approaches in predicting flow separation over thick airfoils and check the compatibility of current μ_t corrections with LE-roughness modeling. The achievement of this aim would fulfill the first steps in the development of a robust numerical method to optimize thick airfoils and improve the energy yield for all surface conditions. An AoA of 0° is selected due to its strong-associated APG on the PS of the airfoil. As measured by Gutierrez et al,[5] the presence of LE roughness implies undesired and abrupt changes in lift and drag for this AoA, which are related to flow separation on the PS of the airfoil. Later, the two corrections on the μ_t of the $k-\omega-SST$ turbulence model from Matyushenko et al[16] and Bangga et al[15] are taken from the literature to analyze their performance along with the modeling LE-roughness cases on thick airfoils. First, the static pressure is measured to check the pressure-coefficient distribution of a 30% thick airfoil. Second, planar PIV measurements have been carried out to determine the velocity fields in the region of the airfoil PS and have a direct comparison with the numerical-2D assumption. From these velocity fields, the mean streamwise velocity, the Reynolds shear stresses, and the a_1 coefficient are retrieved. Afterward, these data are compared with the corresponding numerical results to understand the failure of the RANS equations and determine the effect of the μ_t corrections on the flow magnitudes. Finally, the improvements are quantified from the aerodynamic coefficient perspective at an AoA of 0°. To the authors' knowledge, no empirical validation of these corrections on the mean flow as well as Reynolds shear stresses has been reported in the literature yet. Additionally, there is no research evidence of the compatibility of these corrections with LE-roughness modeling.

The paper is structured as follows. First, the wind tunnel, the airfoil model, the instrumentation, the experimental techniques and the CFD methodology are described in Section 2. Second, the results and their discussion are presented in Section 3. Finally, the concluding remarks are drawn in Section 4.

2 | METHODOLOGY

2.1 | Wind tunnel and airfoil model

Aerodynamic measurements are carried out at the A-tunnel facility of the Delft University of Technology (TU Delft). This is an open-jet closed-circuit vertical wind tunnel. For this experimental campaign, a test section of $0.4\,\mathrm{m} \times 0.7\,\mathrm{m}$ characterized by a contraction ratio of 15:1 is employed, considering a free-stream velocity of $35\,\mathrm{m\,s^{-1}}$. This value is measured through a Pitot-static tube connected to a Mensor DPG 2400 pressure gauge featuring accuracy of 0.03% on the read value.

The turbulence intensity (TI) of the outlet-nozzle flow is below 0.1% for the entire range of operative velocities, as previously demonstrated by Merino et al.[29]

The results presented below use the reference system *XYZ* for the model depicted in Figure 1. The origin $(X=Y=Z=0\mathrm{m})$ is located on the airfoil LE. The *X*-axis is aligned with the streamwise direction, the *Z*-axis with the span direction, and the *Y*-axis is orthogonal to it to form a right-handed coordinate system.

An airfoil model of 30% thickness is tested. It is manufactured using computer numerical-control machining from aluminum with an accuracy of 0.05 mm. Black paint is applied to the model surface to avoid light reflections during the PIV measurements. The airfoil chord length c is 0.25 m, which, in combination with a free-stream velocity of $35\,\mathrm{m\,s^{-1}}$ and a kinematic air viscosity of $1.47 \times 10^{-5}\,\mathrm{m^2\,s^{-1}}$, corresponds to a $Re = 5.95 \times 10^5$. The span length L is 0.4 m, resulting in a span-chord ratio of $L/c = 1.6$. Side plates with a length of 1.2 m are mounted on the sides of the airfoil to ensure two-dimensional flow.

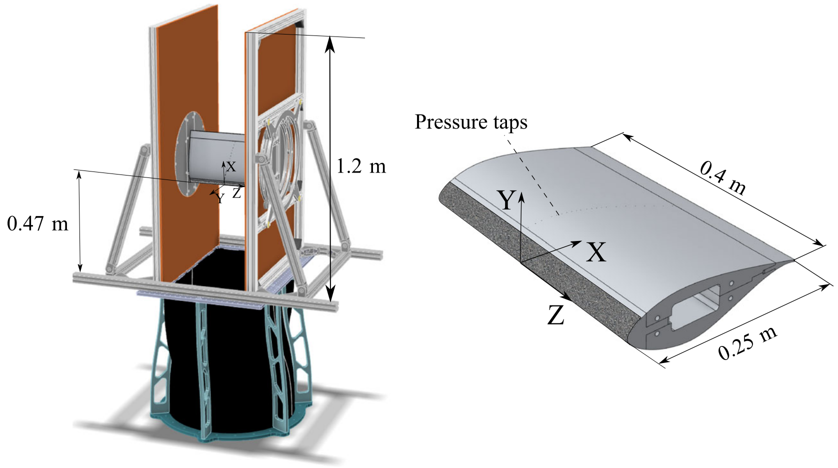

FIGURE 1 Sketch of the test section and model arrangement. The Sandpaper VSM® KK 114 F, corresponding to a grit number of P120, is wrapped around the model LE until the 8% of the chord on both model sides.

2.2 | Pressure-gradient adaptation

The airfoil is tripped on both sides to mimic the APG measured at an AoA of 0 ° for a $Re = 3 \times 10^6$ in the experiments of Gutierrez et al.[5] ($c = 0.6\,\mathrm{m}$; $U_\infty = 75\,\mathrm{ms}^{-1}$), which were then modeled using steady 2D-RANS computations in a following numerical study.[30] The simulations failed in predicting the flow separation independently of the boundary condition used in the LE to emulate roughness. Later, aeroelastic calculations[6] revealed that the operational AoA was 5° at the mid-span region where thick airfoils can be located in case of thick blades. The numerical study[30] demonstrated that the steady 2D-RANS approach mainly fails in predicting the flow separation over the airfoil PS for this AoA of 5°. As already mentioned,[4] this side of the airfoil has a stronger associated APG than the suction side and, therefore, it is selected for validation. Instead of adapting the corresponding APG for an AoA of 5°, 0° is selected to minimize the influence of the open jet of the A-tunnel. As a result, a relatively stronger APG is given at an AoA of 0°, which challenges the validation even more. The experiments of Gutierrez et al[5] constitute the reference for this study because they offer the framework to understand the steady 2D-RANS failure and also quantify the impact of flow separation on the power production of a modern wind turbine.[6] They will be referred to as LSLT in the next part of the paper since they have been conducted at the low-speed low-turbulence wind tunnel of TU Delft.

At the LSLT experiments, two surface configurations were tested. One configuration is denoted as clean and is defined by the airfoil without anything attached to its surface. The other is referred to as rough and allocates sandpaper installed from the LE to the first $8\%c$ on both airfoil sides, c being 0.6 m. This extension is used in the NACA standard method[31] and was the only reference due to the lack of characterization of real LE roughness on wind-turbine blades. The roughness height was chosen in relation to that used for wind-energy purposes in the literature. Kruse et al[11] stated that the surface texture of the first stages of LE erosion has geometrical similarity with sandpapers. They used sandpapers with grit numbers of 40, 120, and 400 for the wind tunnel campaign of a NACA 63_3-418 airfoil with a c of 1 m. Pires et al[32] used sandpapers of P40, P80, and P240 on the same NACA airfoil for a c of 0.6 m. Recently, Nikolov et al[33] have scanned an eroded blade and classified its surface damages with grit numbers ranging from P40 to P180. Finally, sandpaper with a grit number of P100 was selected in the LSLT experiments with a nominal grain size of 162 μm. This roughness height is inside the range of the mentioned studies. However, it is not possible to relate it to a certain state in the blade lifespan due to the stochastic nature of the blade deterioration during operation and the lack of characterization of blade damages.

It is important to mention that the aspect ratios of the airfoil models were 2 for the LSLT experiments and 1.6 for the A-tunnel ones. In accordance with the observations of Crow et al,[34] these values make it possible to avoid the presence of 3D features, like stall cells, once the flow separates and allow a suitable equivalence between both experiments.

To emulate the APG of the LSLT clean case at the A-tunnel experiments while maintaining flow attachment, turbolators are applied to the airfoil PS at $X/c = 0.17$. They are made from carborundum grains with an average height of $k_g = 104\mu\mathrm{m}$ and blown onto a double-sided adhesive tape with 50 μm of thickness and $w_{\mathrm{tur}} = 12\mathrm{mm}$ of width, resulting in a total height of the turbulator of $k_{\mathrm{tur}} = 154\mu\mathrm{m}$, which is designed to meet Braslow's threshold.[35] Additionally, a zig-zag tape with a height of $k_{zz} = 250\mu\mathrm{m}$ and a width of $w_{zz} = 12\mathrm{mm}$ is attached to the SS of the airfoil at $X/c = 0.4$.

In Figure 2A, the C_p is calculated as $C_p = (P - P_\infty)/(0.5\rho U_\infty^2)$, where P is the static pressure, P_∞ is the atmospheric pressure, ρ is the air density, and U_∞ is the magnitude of the free stream velocity. The flow separation on the airfoil PS, once the airfoil is not tripped, is proven by the pressure plateau from $X/c = 0.2$, which does not occur in LSLT conditions. However, the data in Figure 2A confirm the effectiveness of the tripping after suppressing the flow separation on the PS and imposing a similar APG as in the LSLT measurements.

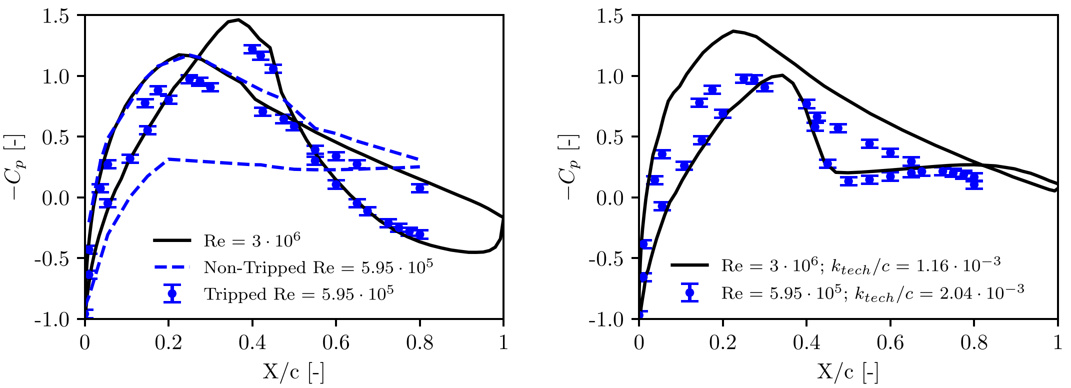

(A) (B)

FIGURE 2 C_p distributions for an AoA of 0°. LSLT measurements, clean case in (A) and rough case in (B), are shown in a black solid line. The dots are shown along with uncertainty bars and correspond to the adaptation at the A-tunnel (grit strips and rescaled sandpaper) to emulate the C_p of the LSLT measurements. The dashed line in (A) corresponds to the A-tunnel measurements without any tripping device on the airfoil surface.

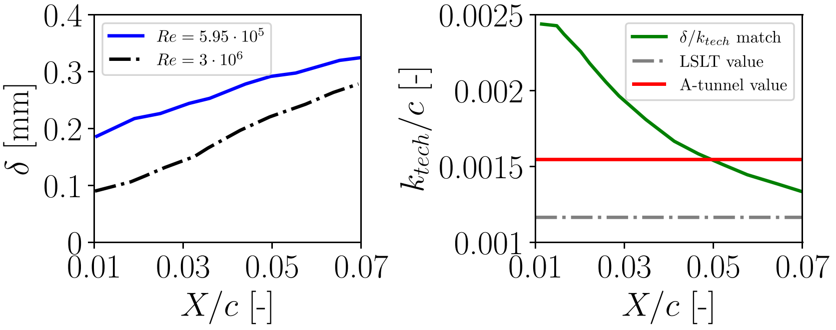

FIGURE 3 On the left, the boundary layer thickness from $k-\omega-SST$ calculations corresponding to the Re of the A-tunnel experiments (blue solid line) and of the LSLT experiments (black dashed-dotted line) are shown. On the right, the gray-dashed-dotted line shows the k_{tech}/c value used in the LSLT measurements. The green line refers to the k_{tech}/c value computed to provide the same δ/k_{tech} as in the LSLT measurements. The red line refers to the final value employed in this study.

Sandpaper is applied on both airfoil sides along the first 8% of c to emulate the rough case of the LSLT measurements. Its selection is based on ensuring the same blockage ratio δ/k_{tech} between the different experimental conditions, where k_{tech} is the maximum roughness height, and δ is the thickness of the BL. Jimenez et al[36] emphasized that δ/k_{tech} defines the region of the BL that is affected by roughness. As shown in Figure 3, fully turbulent computations are performed using the $k-\omega-SST$ turbulence model to compute δ along the sandpaper region. This procedure is applied to the values of U_∞, k_{tech}, and c considered in each tunnel. Subsequently, the value of k_{tech} that meets the desired δ/k_{tech} is derived.

The sandpaper VSM® KK 114 F is finally attached using a double-sided tape with a thickness of 50 μm. Its grit number is P120, which corresponds to an average grain size of $k_s = 125$ μm. An electronic caliper is used to measure a maximum sandpaper thickness of 460 μm. The addition of the thickness of the double-sided tape results in a technical height of $k_{\mathrm{tech}} = 510$ μm.

The effectiveness of the sandpaper rescaling can be assessed in Figure 2B. Indeed, although the C_p value on the SS is not matched, the C_p difference is negligible on the airfoil PS. Moreover, the location of the flow separation at the airfoil PS is the same in both experiments. Upstream of this location, the C_p distributions are almost overlapped.

2.3 | Measurement techniques

2.3.1 | Static-pressure measurement

The static pressure P is measured through 32 differential pressure Honeywell TruStability transducers (range: ±2.5 kPa; accuracy: 12.5 Pa) connected to pressure tap holes with a diameter of 0.4 mm, 14 on the model SS and 18 on the model PS. These are aligned with an inclination of 15°

with respect to the X-axis to avoid flow interference between pressure tap holes, as depicted in Figure 1. The intersection of the holes line with the X-axis is located at $X = 0.5c$. The static pressure is computed by averaging 15 s of data points acquired with a sampling frequency of 50 kHz.

2.3.2 | PIV measurements

Planar PIV measurements are performed in three regions of interest, delimited by the fields of view (FOVs) shown in Figure 4. Previous flow-visualization techniques revealed a 2D flow separation for both LSLT and A-tunnel experiments, which justifies the selection of a planar PIV set up. The FOV (A) includes the rough-to-smooth surface change, whereas the FOV (B) is set to capture the flow acceleration and development near the separation region. The FOV (C) bounds the flow-separation region previously identified in the C_p distribution of the LSLT measurements, as shown in Figure 2B. The dimensions and spanwise distance Z of these FOVs are gathered in Table 1.

A SAFEX Twin-Fog Double Power fog generator is used to produce the seeding of particles from a glycol-based solution. The mean particle diameter is 1 μm. These particles are illuminated by a Quantel EverGreen double-pulse Nd:YAG laser (laser wavelength: 532nm, energy pulse: 70 μJ/pulse). Laser optics are used to obtain a laser sheet with a thickness of around 1mm.

Images are recorded with a LaVision's Imager sCMOS CLHS camera (2560px × 2160px, 16 bit, pixel pitch of 6.5μm). The FOVs (A), (B), and (C) have a dimension of 31mm × 37mm, 108.1mm × 93.85mm, and 103mm × 121mm, respectively. As a result, the magnification per each FOV is 0.45, 0.18, and 0.14, respectively. The cameras are equipped with lenses Nikon AF MICRO NIKKOR with 200mm of focal distance for FOV (A) and with 105mm of focal distance for FOVs (B) and (C). The lens aperture is $f = 11$ for all FOVs. This experimental arrangement makes it possible to ensure a minimum particle size of 2.5 px for all the FOVs, avoiding peak-locking.[37] The FOV (B) is the result of overlapping the recording of two of these cameras, which are set side by side. LaVision's Davis 10.2 software is used to synchronize the cameras and process the images with a sampling frequency of 10Hz.

A multipass cross-correlation algorithm[38] with window deformation[39] is applied to the sequence of images resulting in a spatial resolution of 0.34 mm, 0.8 mm, and 0.43 mm for FOVs (A), (B), and (C), respectively. The final interrogation window size is 24px × 24px, 32px × 32px, 16px × 16px, for FOVs (A), (B), and (C), respectively. For all FOVs, an overlapping factor of 75% is employed. A total number of 1000 uncorrelated pairs of images is used to reach statistical convergence. The PIV parameters per each FOV are summarized in Table 1. The processing of the images is carried out using LaVision's Davis 10.2 software. Finally, spurious vectors are discarded after applying a universal outlier detector.[40] These vectors are replaced by interpolation based on adjacent data.

Random errors in PIV measurements occur because the stochastic nature of turbulence cannot be accurately represented by the cross-correlation analysis used in the PIV processing. Davis's built-in method is used to quantify the uncertainty of random errors along with stochastic errors. This method is based on the comparison of the correlation peak of a pair of interrogation windows that are mapped back to each other.[41] The FOV (C) provides the highest uncertainty values in the mean streamwise velocity component $\bar{u}$, amounting to up to $0.02U_\infty$. Nevertheless, this uncertainty level is given inside the first 30% of the separated shear layer thickness δ_{SS}, whereas it decreases to $0.01U_\infty$ in the rest of the FOV.

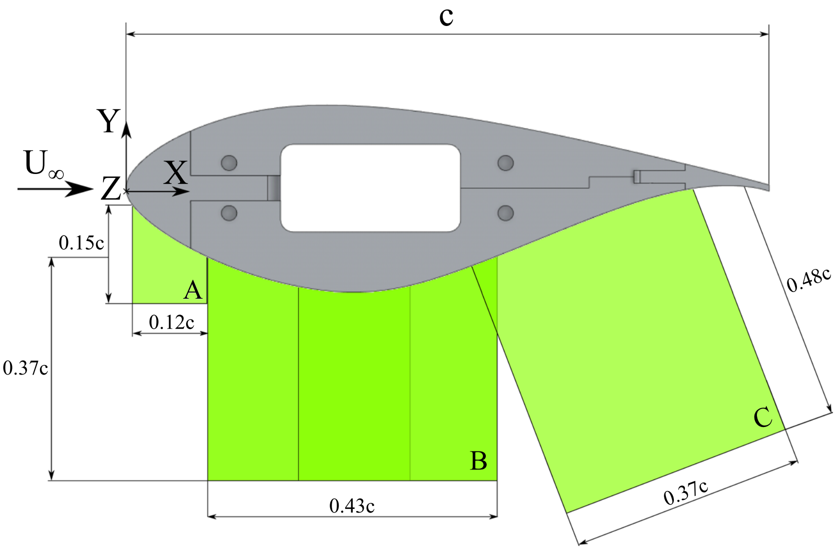

FIGURE 4 FOVs in green along with a sketch of the wind tunnel model. The FOV (B) is the result of two overlapping FOVs.

TABLE 1 PIV parameters for each FOV.

Parameter	FOV (A)	FOV (B)	FOV (C)	Units
Image Rate	10			Hz
Z distance	110	43	46	mm
Pulse time	15	20		µs
Acquisition sensor	2560 × 2160			px × px
FOV width	31	108.1	103	mm
FOV heigth	37	93.85	121	mm
Distance obj-FOV	0.395	0.503	1.10	m
Pixel pitch	6.5			µm
Magnification factor	0.45	0.18	0.14	[-]
f	200	105		mm
f#	11			[-]
Digital resolution	70.36	14	37	px/mm
Windows size	24	32	16	px
Overlap factor	0.75	0.75	0.75	[-]
Spatial resolution	0.34	0.8	0.43	mm
Vector spacing	0.085	0.2	0.11	mm
u_{min}/U_∞	0.003	0.01	0.003	[-]

Note: The Z distance is measured with respect to the origin of the coordinate system defined in Figure 1. u_{min} refers to the minimum resolved velocity.

2.4 | CFD methodology

The CFD results of this study correspond to two different computational domains, one for the LSLT conditions and the other for the A-tunnel conditions whose results are labeled CFD LSLT and CFD A-tunnel, respectively. Both computational domains are defined by an O-grid that extends from the airfoil to a radius of 40*c*, as suggested by Sørensen et al.[42] The first grid is based on the LSLT conditions and was used by Gutierrez et al,[30] for which grid convergence was demonstrated. The grid convergence index (GCI) method[43] was used to choose the mesh resolution. A fine-structured mesh was first obtained following the recommendations provided in previous study.[42] A constant first cell height was employed for each mesh and AoA. Three meshes were built from fine to coarse: L1 with 130,560 cells, L2 with 66,206 cells, and L3 with 16,770 cells. An AoA of 12° was selected to ensure grid convergence for a high-friction velocity, which challenges more the convergence than for lower AoAs. A GCI of 1 was reached for C_L and C_D, which indicated grid convergence, so L1 was selected. Besides, the L1 mesh was modified to meet $y^+_{max} \leq 0.1$ requirements of the roughness BCs because the BL is resolved by the mesh resolution and without using wall functions. Thus, 530 grid points were used to discretize the airfoil geometry, while 270 grid points were used to discretize the flow domain along a normal direction to the airfoil. Even though the computational domain is relatively smaller for the A-tunnel conditions due to the difference in *c*, the same number of grid points was used. Finally, the meshes had 1.4×10^5 cells.

The SIMPLEC algorithm of the open-source CFD solver OpenFOAM v9.0 is used to solve the flow under incompressible and steady assumptions. A second-order linear upwind scheme is used for equations discretization. A residual value lower than 1×10^{-6} is reached for every flow variable, which implied 30,000 iterations. Additionally, a two-dimensional approach is followed using an empty boundary condition on sides normal to the spanwise direction.

The $k-\omega-SST$ turbulence model is used to solve the closure problem of the RANS equations. Wilcox's boundary condition[14] is used along with Hellsten's correction[44] to ensure the proper activation of the SST limiter and emulate the roughness effect on the airfoil LE. Both options are based on the experiments of Nikuradse.[45] Wilcox's boundary condition is applied to the faces that lie on the first 8% *c* on both airfoil sides. A relation $k_s/k_{tech} = 1$ is assumed, so the k_s/c input is 1×10^{-3} for the LSLT conditions and 2.04×10^{-3} for the A-tunnel conditions.

The RANS methodology models the Reynolds shear stresses through the Boussinesq equation, which, for a 2D incompressible flow, can be simplified to

$$-\rho\overline{u'v'} = \mu_t\left(\frac{\partial \bar{u}}{\partial y} + \frac{\partial \bar{v}}{\partial x}\right), \tag{1}$$

where μ_t is a constant of proportionality called eddy viscosity and ρ is the air density. The resolution of the transport equations of the $k-\omega-SST$ turbulence model determines k and ω, which are used to compute μ_t through the expression:

$$\mu_t = \frac{\rho a_1 k}{\max(a_1 \omega; |\mathbf{S}| F_2 F_3)}, \tag{2}$$

$|\mathbf{S}|$ being a scalar measure of the mean strain rate. F_2 and F_3 are blending functions to control the activation of the SST limiter, and a_1 is a constant value equal to 0.31.

As explained in Section 1, this μ_t needs to be corrected to capture the flow separation. Two different corrections are explained in the following sections of this manuscript.

2.4.1 | a_1 method

As mentioned in Section 1, the ratio between the turbulent kinetic energy k and the main turbulent shear stress $\overline{u'v'}$ tends to a constant value of 0.31 at the outer region of the BL. Menter[46] introduced a_1 in the definition of μ_t (see Equation 2) to include the transport effect of $\overline{u'v'}$, which was missed in his previous baseline model $k-\omega$. As a result, the $k-\omega-SST$ turbulence model revealed superior performance for mild-APG flows. However, Klebanoff's experiments were performed on a flat plate with zero-pressure gradient (ZPG) condition, and it is not guaranteed that the a_1 value of 0.31 holds under APGs strong enough to cause flow separation. Regarding Equation (2), an excessive value of a_1 in CFD will increase μ_t and, according to Equation (1), so will the turbulent shear stress. Finally, the capacity of the BL to withstand APG will increase, and the flow separation will not be predicted accurately by CFD.

A straightforward corrective method to implement is to decrease the default value of a_1. A smaller value of a_1 will increase the contribution of the SST limiter (right-hand side in the max operator of Equation 2). Thus, μ_t is lower than when a_1 is set to 0.31 and, consequently, so is the turbulent friction near the wall. Matyushenko et al[16] demonstrated for different airfoils that flow separation is promoted on the airfoil SS as a result. However, the dependency of the a_1 value with the airfoil and the LE-roughness condition needs further justification.

2.4.2 | f_b method

Bangga et al[15] developed a new expression for μ_t (see Equation 3), denoted as μ_t^*, to improve the $k-\omega-SST$ prediction to flow separation over airfoils based on the correction factor f_b:

$$\mu_t^* = f_b \cdot \mu_t. \tag{3}$$

In the following part of the manuscript, the method of Bangga et al[15] will be referred to as the f_b method. This factor is intended to be enabled near the wall and in regions where the flow separates. The inverse of the nearest distance to the wall, that is, $1/y$, is a suitable parameter to regulate the activation of the damping factor. For high values of $1/y$, the corrective factor should be enabled. This inverse wall distance is made non-dimensional with the turbulence length scale $L_t = \sqrt{k}/(\beta^* \omega)$, where β^* is equal to 0.09 like in the original definition of $k-\omega-SST$ turbulence model.[46] Such a length scale is large inside regions of flow separation.

Bangga et al[15] demonstrated that a threshold value of the non-dimensional inverse distance of 2.5 is enough to preserve the turbulence model calibration. Thus, the a_1 value remains equal to 0.31 once this method is used. As a result, the f_b damping factor is defined by

$$f_b = \begin{cases} 0.1 \quad if \quad \dfrac{\sqrt{k}}{(0.09\omega)y} > 2.5 \\ 1 \qquad \text{otherwise} \end{cases} \tag{4}$$

This correction has been implemented in OpenFOAM 9.0 software.

3 | RESULTS

3.1 | Roughness effect on the mean flow

As described by Nikuradse,[45] the main effect of roughness on the mean flow is the introduction of a displacement in the logarithmic layer of the mean-velocity profile. However, there are additional effects to characterize once the boundary layer leaves the airfoil LE and develops over the rest of the smooth surface. Figure 5 shows the evolution of the streamwise velocity component along the airfoil PS. The transition between FOVs

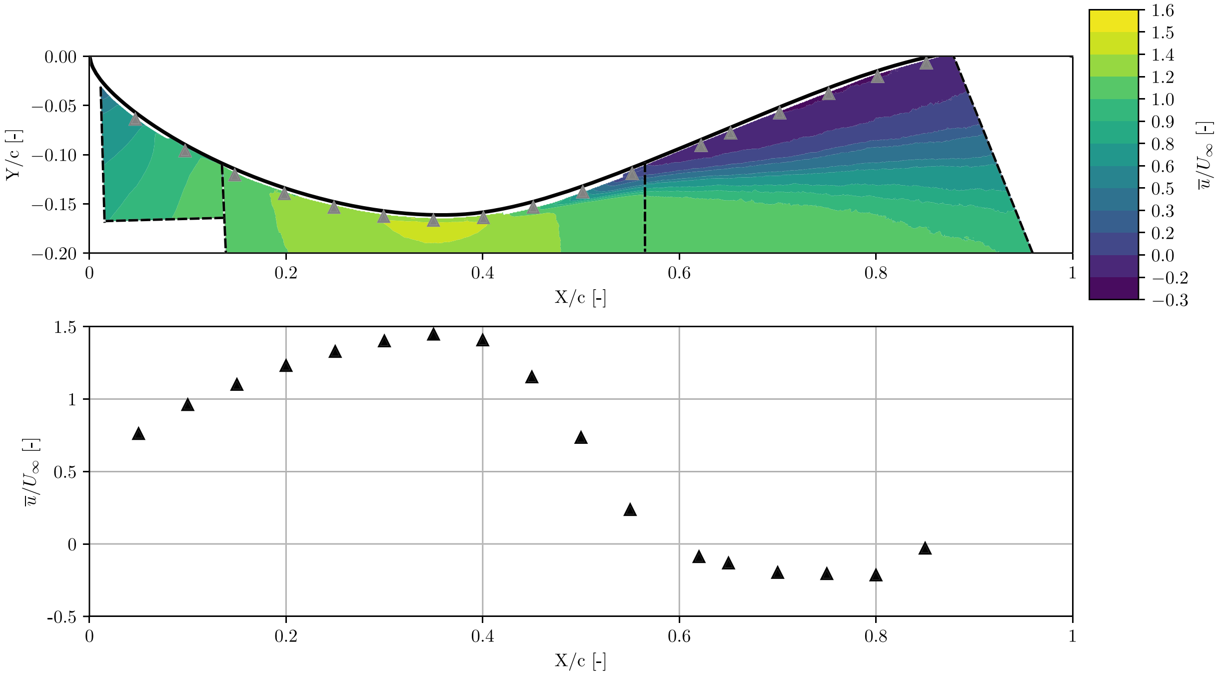

FIGURE 5 Streamwise-velocity component along the airfoil PS for the rough case. The boundaries of each FOV are highlighted with dashed lines. Triangles refer to the points used for the interpolation of $\bar{u}$. These points are offset from the airfoil surface at a distance $d/c = 6 \times 10^{-3}$.

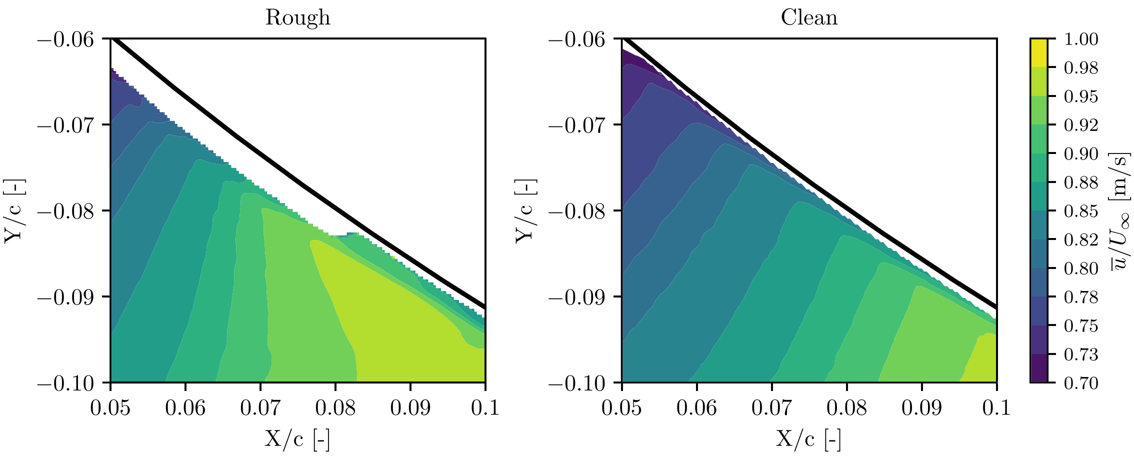

FIGURE 6 Streamwise-velocity component on the airfoil LE for the rough and clean cases.

is smooth despite these regions being acquired at different time periods and spanwise locations during the experiments. This trend confirms that the flow separation is 2D, differently from the 3D flow-separation cases that can be found in the literature.[47]

Regarding the lower plot of Figure 5, the flow acceleration causes the velocity to vary from $0.74U_\infty$ at $X/c = 0.05$ to $1.45U_\infty$ at $X/c = 0.35$. However, for $X/c > 0.35$, the S-shaped of the airfoil PS introduces an adverse-pressure gradient that slows down the flow. The flow separates from the airfoil PS at a streamwise location of $X/c \approx 0.6$. The generated shear layer has a thickness of $0.148c$ at the nearest location to the TE of FOV (C). Furthermore, a recirculation region is found within the shear layer with a thickness of $0.05c$.

Figure 6 shows that the flow experiences a higher acceleration over the sandpaper region than that of the clean case. A velocity deficit of $0.06U_\infty$ is also observed once the flow leaves the sandpaper. This evidence suggests that the sandpaper acts as a backward-facing step. Nevertheless, no recirculation region is identified by the PIV measurements of this study. In the CFD equivalent sand-grain approach, this velocity deficit is not emulated because only a change in boundary condition is placed at the sandpaper end. Unfortunately, the displacement on the logarithmic BL layer cannot be quantified by the PIV measurements due to the fact that, although a high magnification was used, there were not enough vectors in the logarithmic BL layer due to laser reflections. As a result, PIV FOVs are displaced from the airfoil surface at a distance of $0.005c$ over the sandpaper and $0.002c$ over the smooth airfoil.

3.2 | Comparison with RANS simulations

Two different solutions are included in this section: One replicates the mimicking flow conditions (U_∞, k_s, c) at the A-tunnel, whereas the other one those at the LSLT measurements, for which the RANS approach failed to predict flow separation. Figure 7 shows the comparison of the streamwise-velocity profiles at three relevant locations. The normal distance from the airfoil surface d is used to generate these profiles. Regarding the PIV measurements, the flow is almost separated at $X/c = 0.575$ and is characterized by a thicker shear layer at $X/c = 0.7$ and reversed flow. The solution of the RANS equations for the values of U_∞, k_s, and c of the A tunnel slightly overpredicts flow separation for $X/c = 0.5$ and $X/c = 0.575$. However, the agreement with PIV measurements is satisfactory at $X/c = 0.7$. On the other hand, while there is a suitable agreement between the PIV measurements and the result of the LSLT conditions at $X/c = 0.5$, the flow separation is underpredicted for downstream locations. At $X/c = 0.575$, the LSLT solution possesses greater momentum and does not exhibit flow separation. For the last position, the shear layer is approximately 50% thinner than the measured one. These results confirm that the failure of the steady 2D-RANS approach in predicting flow separation depends on the conditions of U_∞, k_s, and c.

Reynolds shear stresses are compared within the separated shear layer at $X/c = 0.7$ (see Figure 8) to further investigate the accuracy of their estimation near the airfoil surface. This is performed at a X/c location where the flow separates because the separated layer is thick enough to include the Reynolds shear-stress peak in the PIV measurements. Only three components, that is, $\overline{u'^2}, \overline{v'^2}$, and $\overline{u'v'}$, are compared due to the 2D assumption of the flow. Two CFD solutions are included in the comparison depending on whether the values of U_∞ and k_s correspond to A-tunnel experiments or LSLT experiments. For both CFD solutions, the most significant deviation with respect to the PIV measurements is given by the component $\overline{u'^2}$, which is the variance of the streamwise velocity. For the $\overline{v'^2}$ component, the difference is significantly reduced, whereas the error of $\overline{u'^2}$ is implicitly included in the main-shear stress $\overline{u'v'}$. Similarly, Jianghua et al[48] demonstrated with PIV measurements that RANS approaches

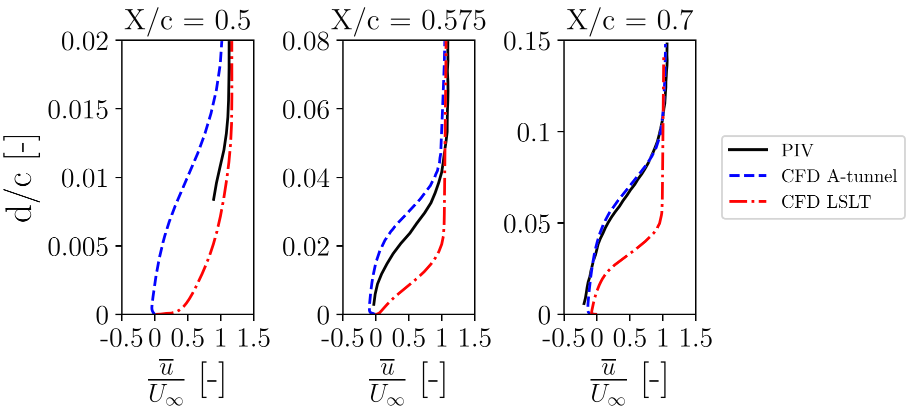

FIGURE 7 Comparison of streamwise-velocity profiles at several X/c locations between CFD and PIV. CFD A-tunnel refers to the results corresponding to the conditions of U_∞, k_s, and c used at the A-tunnel. CFD LSLT refers to the results corresponding to the conditions of U_∞, k_s, and c used at the LSLT.

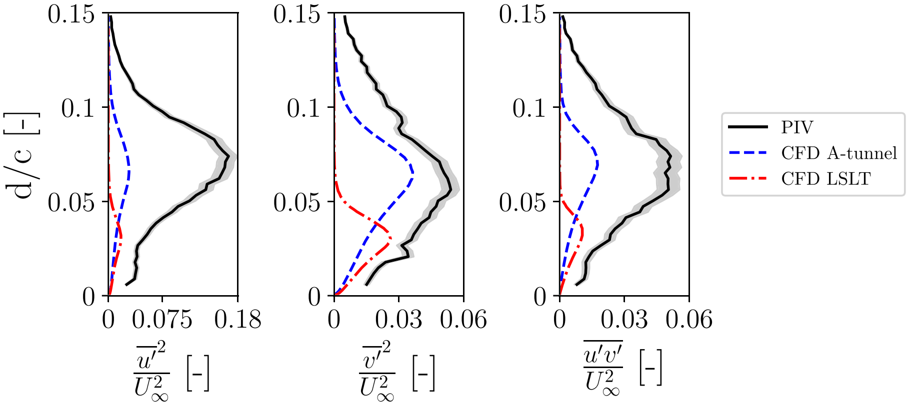

FIGURE 8 Comparison of Reynolds shear-stresses profiles between CFD and PIV at $X/c = 0.7$. Reynolds shear stresses are normalized with U_∞^2. CFD A-tunnel refers to the results corresponding to the conditions of U_∞, k_s, and c used at the A-tunnel. CFD LSLT refers to the results corresponding to the conditions of U_∞, k_s, and c used at the LSLT experiments.

underpredict the components of $\overline{u'}^2$ and $\overline{u'v'}$ inside the region of trailing-edge separation of an A-airfoil, whereas hybrid LES/RANS methods were able to enhance the prediction.

The d/c location of the peak value of all the Reynolds shear-stresses components matches the CFD results related to the A-tunnel conditions, whereas a lower location of this peak is given when the U_∞ and k_s are set to match the LSLT experiments. As a result, there is an overestimated contribution of the Reynolds shear stresses and, in turn, the turbulent mixing near the wall. Thus, the flow does not separate, as supported by the velocity profiles in Figure 7. A correction of μ_t is hence required to improve the estimation of the Reynolds shear stresses when the LSLT conditions are used.

3.3 | Correction of the CFD solution

This section collects the results of correcting the solution of the RANS equations with the flow conditions of LSLT. The correction is performed using the two different methods mentioned in Section 2.4.

3.3.1 | Results for the a_1 method

Following the a_1 method, the constant a_1 has varied from 0.31 to 0.28 with a decrement of 0.01 as performed by Matyushenko et al.[16] For their case, the optimal value of a_1 was equal to 0.28 for the kind of airfoil they analyzed. However, Figure 9 exhibits a significant variation in the velocity profile for small changes in a_1. For this thick-airfoil case, an optimization process based on the least squares method revealed an optimal a_1 value of 0.29. Thus, a significant airfoil dependency is shown with this method.

On the other hand, Figure 10A shows the a_1 value retrieved from FOV B as the ratio between $\overline{u'v'}$ and the turbulent kinetic energy k, which is far from being constant as assumed in the $k-\omega-SST$ model and varies in the streamwise direction and the direction normal to the airfoil surface. From $X/c \approx 0.425$, the value of a_1 rises from ≤ 0.18 to approximately 0.36. In the normal direction, the value is, on average, around 0.29 but increases up to 0.36 near the location of flow separation. Figure 10B,C shows the velocity and a_1 profiles extracted at $X/c = 0.5$ before the flow separates. A wrong value for this location in CFD would overestimate the Reynolds shear stresses, causing the flow to remain attached downstream. The profile of the velocity component tangential to the airfoil u_η is shown in Figure 10B to visualize the region of the boundary layer where a_1 ranges between 0.27 and 0.3. Bands of d/δ are incorporated in Figure 10A to corroborate the interpolation of the a_1 profile of Figure 10C, where δ refers to the BL thickness computed at $X/c = 0.5$. Special attention must be paid near the outer edge of the boundary layer, where Townsend[19] and Bradshaw[18] showed that a_1 tends to 0.31 for a ZPG boundary layer. In this case, for an APG boundary layer, the value of a_1 varies between 0.27 and 0.29 just before the outer edge of the boundary layer ($0.88 < d/\delta < 0.95$).

This result is in close agreement with the work of Aubertine and Eaton[21] and Alving and Fernholz.[20] Aubertine's measurements demonstrated that a_1 decreases to approximately 0.28 near the outer edge of boundary layers subjected to APG. Bradshaw[18] justified that the APG drops the a_1 value because it introduces irrotational motions at the outer edge of the BL, which are comparable in intensity to turbulent fluctuations. Aubertine and Eaton[21] also demonstrated that the value of 0.31 was recovered for a_1 once the boundary layer left the APG region and faced another ZPG region. Alving and Fernholz[20] also reported that approaching the flow separation, a_1 drops along the BL ($d/\delta > 0.5$), while small

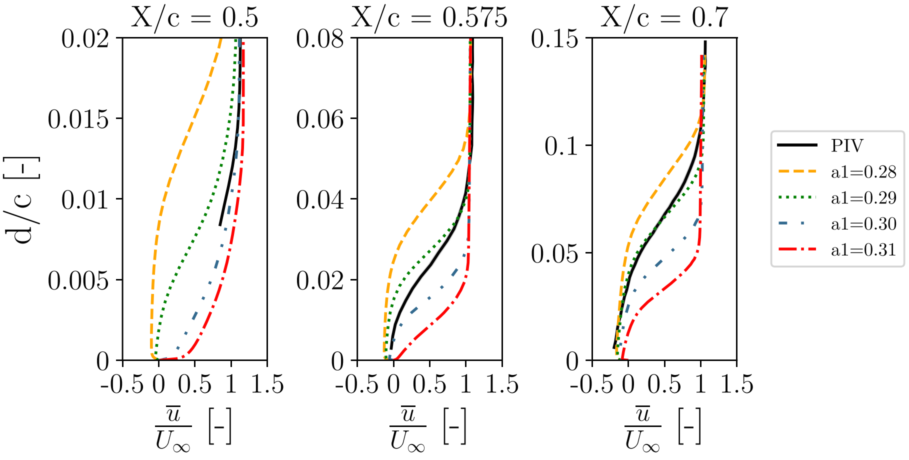

FIGURE 9 Comparison of streamwise-velocity profiles for several values of a_1. CFD replicates the testing conditions of LSLT experiments.

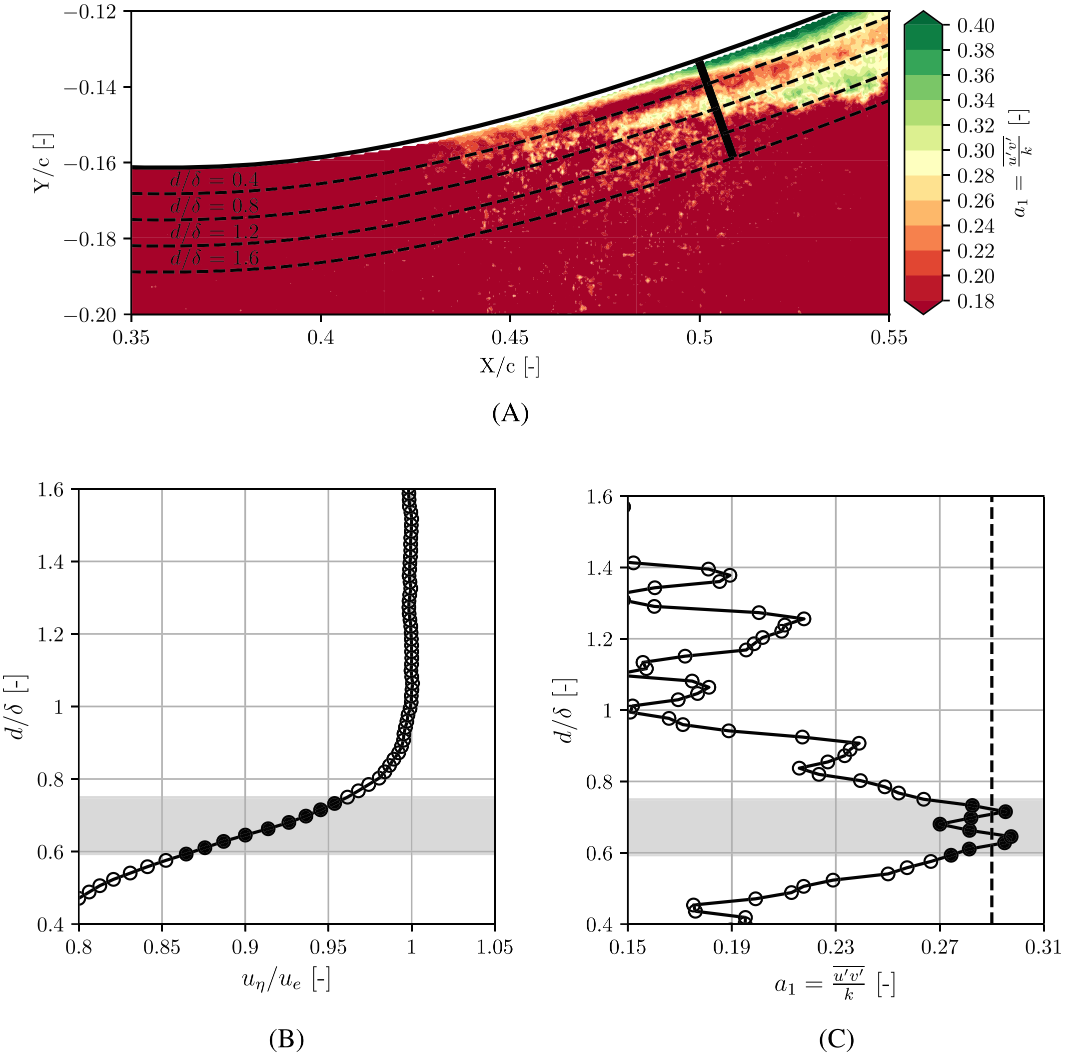

(A)

(B)

(C)

FIGURE 10 PIV results. (A) Contour plot of a_1 near the location of flow separation. Dashed lines indicate a constant d/δ where δ is the boundary layer thickness retrieved at $X/c = 0.5$. The thickest solid line refers to the normal direction to the airfoil surface at $X/c = 0.5$. (B) Non-dimensional profile of the tangential velocity u_η extracted at $X/c = 0.5$. u_e is the edge velocity. (C) Profile of a_1 along the boundary layer extracted at $X/c = 0.5$. The gray bands and filled points indicate an a_1 value between 0.27 and 0.3. The dashed-vertical line indicates a a_1 value of 0.29.

values of a_1 were measured in the inner layer of the BL. Georgiadis and Yoder[22] used Drivers experiments[49] in an axisymmetric diffuser to demonstrate that a_1 remains below 0.31 throughout the diffuser. However, the studies mentioned in Section 1 are based on flat plate flows as well as axisymmetric-diffuser flows, and no evidence of the a_1 value was reported for flow separation over airfoils.

3.3.2 | Results for the f_b method

The local method of Bangga et al[15] is compared with the optimal a_1 modification, which amounts to $a_1 = 0.29$. Figure 11 shows that the f_b method decreases the momentum near the wall for all the X/c locations evaluated. This demonstrates the appropriate activation of the damping factor within the separation region while keeping out of it the original RANS solution. As a result, the RANS computations with the LSLT conditions feature a better agreement with the PIV measurements. Both corrections significantly improve the prediction of the velocity profile at $X/c = 0.5$, confirming the relevance of correcting μ_t before the flow separation. The overall improvement of the f_b method is in the same order of magnitude as the a_1 method. For a distance $d/c \leq 0.02$ at $X/c = 0.575$ and $X/c = 0.7$, there is reversed flow. This is more prominent in the f_b method rather than the numerical results with the a_1 method and the PIV measurements.

Figure 12 demonstrates that both RANS corrections decrease the contribution near the wall of all the Reynolds shear stresses, which is known to enhance flow separation. This is identified in Figure 12 by the displacement of the maximum peak in the Reynolds shear-stresses profiles. Additionally, the application of these corrections enhances the accuracy of the results of Gutierrez et al.[30] Both solutions are almost identical

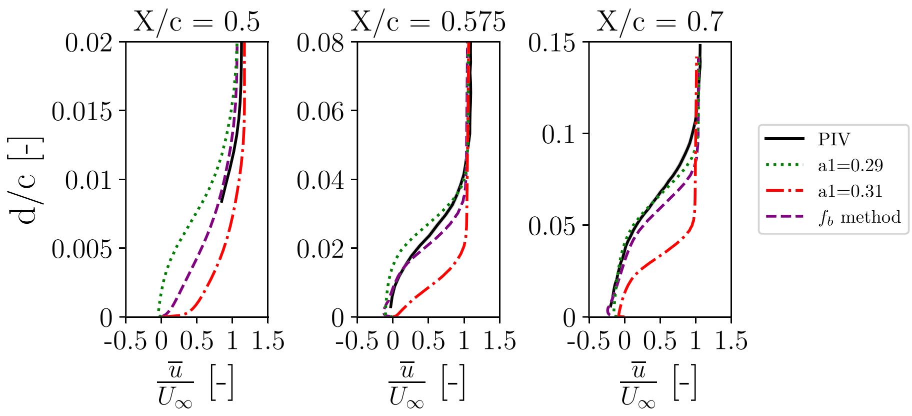

FIGURE 11 Comparison of streamwise-velocity profiles at several X/c locations between the CFD and the PIV results. The CFD results correspond to the testing conditions of the LSLT experiments.

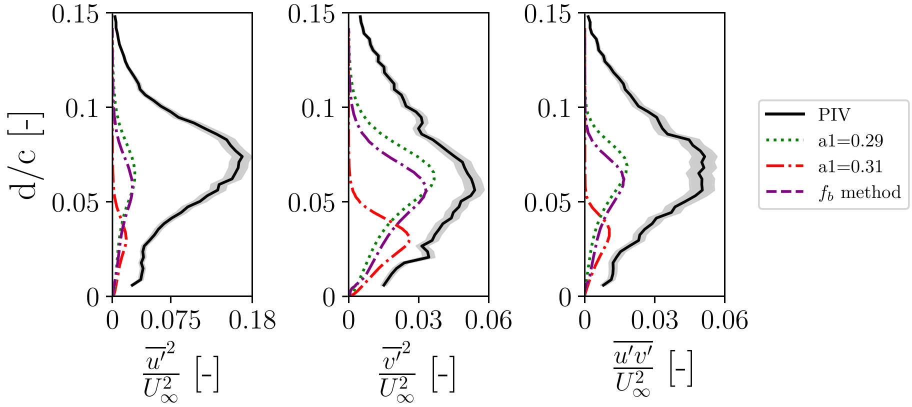

FIGURE 12 Comparison of Reynolds shear-stresses profiles between CFD and PIV at $X/c = 0.7$. The CFD results correspond to the testing conditions of the LSLT experiments. The solid black lines refer to the data from PIV, which are represented with gray bands of uncertainty.

to the solution of the RANS equations given by the values of U_∞ and k_s of the A-tunnel. Thus, the correction on μ_t improves the trend of Reynolds shear stress, resulting in the same d/c locations of their maximum value as those measured with PIV. This correspondence validates the threshold of 2.5 used for L_t in Equation (3), which was based only on numerical validation in the work of Bannga et al.[15] The reduction of the stress values near the wall ($d/c < 0.025$) improves the mean-velocity prediction, as shown in Figure 11.

It is not possible to carry out a PIV validation of the f_b method as done for the a_1 method in Figure 10. This method is based on damping μ_t, which is not a physical quantity. One option could be to retrieve μ_t using Equation (1) using the PIV data. Nevertheless, Beresh et al[27] reported the challenges in retrieving μ_t from PIV data due to high-frequency noise as well as random and biased errors in computing the strain rate of the mean-velocity field.

The only physical magnitude used by the method is the turbulent length scale L_t, which depends on k and the dissipation rate ω. Nonetheless, this length scale is challenging to be retrieved from PIV, since it depends on ω, which is a third-order statistic and would imply a significant number of PIV data to reach statistical convergence. In addition, the challenges would be as similar as for μ_t because ω depends on the derivatives of the velocity fluctuations.

3.3.3 | Results of the aerodynamic coefficients

The Reynolds shear stresses modeled by the RANS equations determine the development of the flow around the airfoil and, in turn, the evolution of the pressure distribution on its surface. The integration of the latter quantity along the blade span is directly related to the torque and thrust produced by the wind turbine. Thus, a wrong modeling of the Reynolds shear stresses would imply a wrong prediction of the C_p distribution as well as the wind turbine performance.

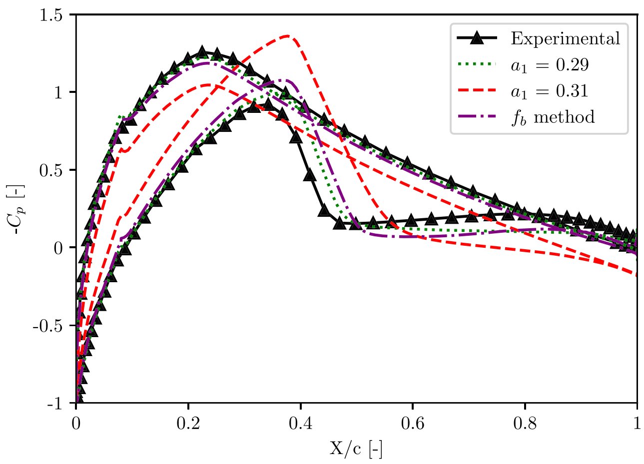

FIGURE 13 C_p for an AoA of 0.

TABLE 2 Aerodynamic-coefficient results for an AoA of 0°.

Method	C_M	C_D	C_L
Experimental	−0.013	0.066	0.334
$a_1 = 0.31$	−0.012	0.028	0.073
$a_1 = 0.29$	−0.023	0.040	0.325
f_b method	−0.018	0.037	0.274

Figure 13 compares the C_p distribution at an AoA of 0° with and without the RANS corrections to capture the flow separation. The experimental data come from the LSLT tests. The default value of $a_1 = 0.31$ refers to the RANS calculation without any correction. A significant improvement is found once a_1 is changed to 0.29 or is kept at 0.31 but using the f_b method. Both corrections provide a similar prediction of C_p on the SS and a slightly different one on the PS. Table 2 includes the value of the numerical and experimental aerodynamic coefficients for an AoA of 0°. Regarding these values, the default RANS setup with a_1 equal to 0.31 provides an error of 78% for the lift coefficient C_L and 58% for the drag coefficient C_D. Changing the a_1 value from 0.31 to 0.29 reduces the C_L error by 75%, with a total error of 3%, whereas the f_b method reduces it by 60%. On the other hand, both methods decrease the error in the drag estimation by 18% and 14% for the a_1 method and f_b method, respectively.

4 | CONCLUSIONS

This study contributes to the understanding of the failure in the steady 2D-RANS equations to predict flow separation caused by LE roughness on a 30% thick airfoil and provides knowledge to extend the current μ_t corrections. The numerical modifications driven by these corrections are justified with measurements of different flow magnitudes and are demonstrated to be compatible under rough LE conditions. Static-pressure measurements have been carried out to ensure an appropriate pressure distribution of the airfoil that induces flow separation on the airfoil PS. Additionally, planar PIV measurements have been performed to validate the effect of μ_t corrections on the mean streamwise velocity and Reynolds shear stresses. These measurements also allow clarifying how LE roughness can be emulated in wind-tunnel experiments. The influence of the RANS equations on the values of U_∞, k_s, and c demonstrates the crucial role played by the eddy-viscosity correction in accurately predicting flow separation. Two different corrections are studied, that is, the modification of the calibration coefficient a_1 and the introduction of a local damping factor f_b. The results discussed in this research work significantly contribute to the development of these corrections, which were only validated in the literature using measurements of aerodynamic coefficients.

The following conclusions can be drawn:

- This paper contributes with a characterization of the sandpaper effect on the mean flow, which opens up future research on LE-roughness emulation in wind-tunnel testing. Figure 6 demonstrates that the flow experiences a higher acceleration over the sandpaper than the smooth LE and then faces a velocity deficit similar to the backward-facing step. Similar PIV measurements could be performed in the future for a replicated wind-turbine-blade roughness to check the similarity of its effect on the flow with that from the sandpaper.

- The solution of the RANS equations captures the reversed flow when U_∞ is equal to that of the A-tunnel experiments. However, there is no flow separation for the experimental LSLT conditions that are characterized by a greater value of U_∞. The PIV measurements performed in this study corroborate the overestimation of the Reynolds shear stresses near the airfoil surface for the experimental LSLT conditions. Due to the contribution of the Reynolds shear stresses in the RANS momentum equation, their overestimation due to a wrong μ_t near the airfoil surface provides the wrong modeling of the mean flow and the underestimation of flow separation, as shown in Figure 8 for all of their components.
- The results of this study demonstrate that the wrong estimation of the Reynolds shear stresses, especially for the $\overline{u'}^2$ and $\overline{u'v'}$ components, as found by Jianghua et al[48] for a smooth airfoil, also holds downstream of LE roughness. Bangga et al[15] showed numerically that the studied corrections on μ_t displace the location of the Reynolds shear-stresses peak from the airfoil surface, and the PIV measurements seem to confirm the need for this displacement. However, these corrections on μ_t do not suffice to match the PIV value of the shear stresses and need further investigation.
- Although most of the literature about the a_1 drop for APG flows is based on flat plates and diffusers, the PIV measurements presented above contribute to the characterization of the a_1 drop near the flow-separation region of a thick airfoil. The a_1 value is demonstrated not to be constant, as instead assumed in the turbulence model formulation. On the other hand, the CFD results for the a_1 method demonstrate a significant sensitivity on the velocity profiles with minor changes in a_1. In this case, an optimal a_1 value of 0.29, which is correlated to the PIV measurements, is found. This value differs from that determined by Matyushenko et al[16] for other airfoils under smooth conditions. Thus, the method is dependent on the airfoil and the flow conditions.
- The f_b method is shown to work along with boundary conditions to emulate roughness on the airfoil LE. Its local behavior makes the f_b factor act only inside the flow separation region. A relatively larger region of reverse flow is reported near the airfoil surface for this method, which deserves further investigation.

Finally, the assessment carried out in this research work shows that the a_1 method reduces the error of the estimation of the C_L by 75% but is an airfoil-dependent method. To avoid this dependency, further research is required for the value of a_1 under different APGs and airfoil locations. On the other hand, the f_b method reduces the C_L error slightly less, that is, by 20%, but has a significant advantage because is not airfoil-dependent. Thus, the validation carried out in this study shows that current μ_t corrections can also improve the prediction of the aerodynamic impact caused by LE roughness at the studied APG conditions. However, the drawn conclusions need further investigation to correlate them with other APG conditions, which will depend on *Re*, AoAs, airfoil models, and types of LE roughness.

ACKNOWLEDGEMENTS

We are grateful to Nordex SE, TU-Delft and UPNA for providing the necessary support to carry out this research.

DATA AVAILABILITY STATEMENT

Author elects to not share data.

ORCID

Ruben Gutierrez https://orcid.org/0000-0003-1471-9668
Riccardo Zamponi https://orcid.org/0000-0001-5172-6109
Daniele Ragni https://orcid.org/0000-0002-8014-5650
Elena Llorente https://orcid.org/0000-0001-7759-2241

PEER REVIEW

The peer review history for this article is available at https://www.webofscience.com/api/gateway/wos/peer-review/10.1002/we.2822.

REFERENCES

1. Timmer WA, Bak C. *Advances in Wind Turbine Blade Design and Materials*: Woodhead Publishing; 2013.
2. Corten GP. *Flow Separation on Wind Turbines Blades*: Utrecht University; 2001.
3. Kelly J, Vogel C, Willden R. Impact and mitigation of blade surface roughness effects on wind turbine performance. *Wind Energy*. 2022;25(4):660-677. doi:10.1002/we.2691
4. Timmer W, Schaffarczyk A. The effect of roughness at high Reynolds numbers on the performance of aerofoil DU 97-w-300mod. *Wind Energy*. 2004; 7:295-307. doi:10.1002/we.136
5. Gutiérrez R, Llórente E, Echeverría F, Ragni D. Wind tunnel tests for vortex generators mitigating leading-edge roughness on a 30% thick airfoil. *Journal of Physics: Conference Series*. 2020;1618(5):52058. doi:10.1088/1742-6596/1618/5/052058
6. Gutiérrez R, Llorente E, Ragni D. Induced stalled flow due to roughness sensitivity for thick airfoils in modern wind turbines. *Journal of Physics: Conference Series*. 2022;2151(1):12001. doi:10.1088/1742-6596/2151/1/012001
7. Ramanujam G, Ozdemir H. Improving airfoil lift prediction. *35th Wind Energy Symposium*. 2017. doi:10.2514/6.2017-1999
8. Ramanujam G, Ozdemir H, Hoeijmakers HW. Improving airfoil drag prediction. *34th Wind Energy Symposium*. 2016. doi:10.2514/6.2016-0748

9. Olsen AS, Ramos-García N, Bak C. Improved roughness model for turbulent flow in 2d viscous-inviscid panel methods. *Wind Energy*. 2020;23(3): 608-616. doi:10.1002/we.2445
10. Langel CM, Chow R, Hurley OF, Dam CaseCPPVan, Maniaci DC, Ehrmann RS, White EB. Analysis of the impact of leading edge surface degradation on wind turbine performance. *33rd Wind Energy Symposium*. 2015; January:1-13. doi:10.2514/6.2015-0489
11. Krog Kruse E, Bak C, Olsen AS. Wind tunnel experiments on a NACA 633-418 airfoil with different types of leading edge roughness. *Wind Energy*. 2021;24(11):1263-1274. doi:10.1002/we.2630
12. Sezer-Uzol N, Uzol O, Orbay-Akcengiz E. *CFD Simulations for Airfoil Polars*: Springer International Publishing; 2020.
13. Sørensen NN, Olsen AS, Bak C, Gaunaa M, Beckerlee JS, Fischer A, Mikkelsen RF, Ildvedsen S. CFD modeling of the Poul la Cour tunnel. *Journal of Physics: Conference Series*. 2020;1618(5):52047. doi:10.1088/1742-6596/1618/5/052047
14. Wilcox DC. *Turbulence Modelling for CFD 3rd edition*: D C W Industries, Canada, CA, USA, pp. 182-185; 2006.
15. Bangga G, Kusumadewi T, Hutomo G, Sabila A, Syawitri T, Setiadi H, Faisal M, Wiranegara R, Hendranata Y, Lastomo D, Putra L, Kristiadi S. Improving a two-equation eddy-viscosity turbulence model to predict the aerodynamic performance of thick wind turbine airfoils. *Journal of Physics: Conference Series*. 2018;974. doi:10.1088/1742-6596/974/1/012019
16. Matyushenko AA, Garbaruk AV. Adjustment of the k-ω SST turbulence model for prediction of airfoil characteristics near stall. *Journal of Physics: Conference Series*. 2016;769(1). doi:10.1088/1742-6596/769/1/012082
17. Zhong W, Tang H, Wang T, Zhu C. Accurate RANS simulation ofwind turbine stall by turbulence coefficient calibration. *Applied Sciences (Switzerland)*. 2018;8(9). doi:10.3390/app8091444
18. Bradshaw P. The turbulence structure of equilibrium boundary layers. *Journal of Fluid Mechanics*. 1967;29(4):625-645. doi:10.1017/S0022112067001089
19. Townsend AA. *The Structure of Turbulent Shear Flow*. 2nd ed., Vol. 56: Cambridge University Press; 1976.
20. Alving AE, Fernholz HH. Turbulence measurements around a mild separation bubble and downstream of reattachment. *Journal of Fluid Mechanics*. 1996;322:297-328. doi:10.1017/S0022112096002807
21. Aubertine CD, Eaton JK. Turbulence development in a non-equilibrium turbulent boundary layer with mild adverse pressure gradient. *Journal of Fluid Mechanics*. 2005;532:345-364. doi:10.1017/S0022112005004143
22. Georgiadis N, Yoder D. Recalibration of the shear stress transport model to improve calculation of shock separated flows. *51st AIAA Aerospace Sciences Meeting including the New Horizons Forum and Aerospace Exposition*. 2013. doi:10.2514/6.2013-685
23. Wu W, Piomelli U. Effects of surface roughness on a separating turbulent boundary layer. *Journal of Fluid Mechanics*. 2018. doi:10.1017/jfm.2018.101
24. Song S, Eaton J. The effects of wall roughness on the separated flow over a smoothly contoured ramp. *Experiments in Fluids*. 2002;33(1):38-46. doi:10.1007/s00348-002-0411-1
25. Tay G, Kuhn D, Tachie M. Adverse and favourable pressure gradient turbulent flows over smooth and rough surfaces. *39th AIAA Fluid Dynamics Conference*. 2009. doi:10.2514/6.2009-4046
26. Mottaghian P, Yuan J, Piomelli U. Boundary layer separation under strong adverse pressure gradient over smooth and rough walls. *Springer International Publishing*. 2018;24. doi:10.1007/978-3-319-63212-4_21
27. Beresh SJ, Miller NE, Smith B. Practical challenges in the calculation of turbulent viscosity from PIV data. *Aerodynamic Measurement Technology and Ground Testing Conference*. 2018. doi:10.2514/6.2018-2987
28. Zhang Y. Effects of distributed leading-edge roughness on aerodynamic performance of a low-Reynolds-number airfoil: an experimental study. *Theoretical and Applied Mechanics Letters*. 2018;8(3):201-207. doi:10.1016/j.taml.2018.03.010
29. Merino-Martínez R, Rubio Carpio A, Lima Pereira LT, van Herk S, Avallone F, Ragni D, Kotsonis M. Aeroacoustic design and characterization of the 3D-printed, open-jet, anechoic wind tunnel of Delft University of Technology. *Applied Acoustics*. 2020;170:107504. doi:10.1016/j.apacoust.2020.107504
30. Gutiérrez R, Llorente E, Ragni D, Aranguren P. Study on k$-\omega$ shear stress transport corrections applied to airfoil leading-edge roughness under RANS framework. *Journal of Fluids Engineering*. 2022;144(4). doi:10.1115/1.4052925
31. Abbott IH, Von Doenhoff AE. Theory of wing sections: including a summary of airfoil data. *Press*. 1959.
32. Pires O, Munduate X, Boorsma K, Ceyhan Yilmaz O, Aa Madsen H, Timmer WA. Experimental investigation of surface roughness effects and transition on wind turbine performance. *Journal of Physics: Conference Series*. 2018;1037(5). doi:10.1088/1742-6596/1037/5/052018
33. Nikolov. I, Madsen. C. Quantifying wind turbine blade surface roughness using sandpaper grit sizes: an initial exploration. *Proceedings of the 16th International Joint Conference on Computer Vision, Imaging and Computer Graphics Theory and Applications*. 2021;5:801-808. doi:10.5220/0010283908010808
34. Crow SC. Stability theory for a pair of trailing vortices. *AIAA Journal*. 1970;8(12):2172-2179. doi:10.2514/3.6083
35. Braslow A, Hicks R, Harris R. Use of grit-type boundary-layer-transition trips on wind-tunnel models. *NASA Technical Note (TN)*. 1966.
36. Jiménez J. Turbulent flows over rough walls. *Annual Review of Fluid Mechanics*. 2004. doi:10.1146/annurev.fluid.36.050802.122103
37. Raffel M, Willert C, Wereley S, Kompenhans J, Raffel M, Willert CE, Wereley S, Kompenhans J. *Particle Image Velocimetry: A Practical Guide*: Springer International Publishing; 2013.
38. Scarano F, Riethmuller ML. Advances in iterative multigrid PIV image processing. *Experiments in Fluids*. 2000;29(1):S051-S060. doi:10.1007/s003480070007
39. Scarano F. Iterative image deformation methods in PIV. *Measurement Science and Technology*. 2001;13(1):R1-R19. doi:10.1088/0957-0233/13/1/201
40. Westerweel J, Scarano F. Universal outlier detection for PIV data. *Experiments in Fluids*. 2005;39(6):1096-1100. doi:10.1007/s00348-005-0016-6
41. Wieneke B. PIV uncertainty quantification from correlation statistics. *Measurement Science and Technology*. 2015:11. doi:10.1088/0957-0233/26/7/074002
42. Sørensen NN, Méndez B, Munoz A, Sieros G, Jost E, Lutz T, Papadakis G, Voutsinas S, Barakos GN, Colonia S, Baldacchino D, Baptista C, Ferreira C. CFD code comparison for 2d airfoil flows. *Journal of Physics: Conference Series*. 2016;753(8):82019. doi:10.1088/1742-6596/753/8/082019
43. Roache PJ. Quantification of uncertainty in computational fluid dynamics. *Annual Review of Fluid Mechanics*. 1997;29(1):123-160. doi:10.1146/annurev.fluid.29.1.123
44. Hellsten A, Laine S. Extension of the k-ω-SST turbulence model for flows over rough surfaces. *22nd Atmospheric Flight Mechanics Conference*. 1997: 252-260. doi:10.2514/6.1997-3577

45. Nikuradse J. Laws of Flow in Rough Pipes. 4, Washington November, National Advisory Committee for Aeronautics; 1936.
46. Menter F. Zonal two equation k-w turbulence models for aerodynamic flows. *23rd Fluid Dynamics, Plasmadynamics, and Lasers Conference*. 1993. doi:10.2514/6.1993-2906
47. Ragni D, Ferreira C. Effect of 3d stall-cells on the pressure distribution of a laminar NACA64-418 wing. *Experiments in Fluids*. 2016;57(8):127. doi:10.1007/s00348-016-2215-8
48. Ke J, Edwards J. RANS and les/RANS simulation of airfoils under static and dynamic stall. *51st AIAA Aerospace Sciences Meeting including the New Horizons Forum and Aerospace Exposition*. 2013. doi:10.2514/6.2013-955
49. Driver D. Reynolds shear stress measurements in a separated boundary layer flow. *22nd Fluid Dynamics, Plasma Dynamics and Lasers Conference*. 1991. doi:10.2514/6.1991-1787

How to cite this article: Gutierrez R, Zamponi R, Ragni D, Llorente E, Aranguren P. On the extension of $k{-}\omega{-}SST$ corrections to predict flow separation on thick airfoils with leading-edge roughness. *Wind Energy*. 2023;1-18. doi:10.1002/we.2822

APPENDIX A: NOMENCLATURE

Variable	Units	Meaning
C_p	-	Pressure coefficient
k_s	m	Equivalent sand grain height
k_{tech}	m	Technical sand grain height
k_g	m	Average sandpaper grain height
k_{tur}	m	Average grain height of grit strip
k_{zz}	m	Height of zig-zag tape
f_b	-	Damping factor of eddy viscosity
f	m	Focal length
f	-	Lens aperture
μ_t	$m^2\ s^{-1}$	Eddy viscosity
μ_t^*	$m^2\ s^{-1}$	Modified eddy viscosity
$\overline{u'}^2, \overline{v'}^2, \overline{u'v'}$	Pa	Reynolds shear stresses
k	$m^2\ s^2$	Turbulent kinetic energy
a_1	-	Ratio between $\overline{u'v'}$ and k
TI	-	Turbulence intensity
L	m	Span length of airfoil model
L_t	m	Turbulent length scale
c	m	Airfoil chord length
Re	-	Reynolds number based on c
U_∞	m/s	Free-stream velocity
w_{tur}	m	Width of the grit strip
w_{zz}	m	Width of zig-zag tape
ρ	kg/m^3	Air density
P_∞	Pa	Free-stream pressure
δ	m	Boundary layer thickness
ω	s^{-1}	Specific dissipation rate
d	m	Normal wall distance
β^*	-	Empirical constant of the $k-\omega-SST$ turbulence model
$\bar{u}$	-	Averaged-streamwise velocity component
$\bar{v}$	-	Averaged-normal velocity component

(Continues)

Variable	Units	Meaning
u_η	m/s	Tangential velocity component
u_e	m/s	Edge velocity component
$\lvert\mathbf{S}\rvert$	s^{-1}	Being a scalar measure of the mean strain rate
F_2, F_3	-	Blending functions of the $k-\omega-SST$ turbulence model
C_L	-	Lift coefficient
C_D	-	Drag coefficient
C_M	-	Momentum coefficient